

# Controlled patterning of crystalline domains by frontal polymerization

<https://doi.org/10.1038/s41586-024-07951-7>

Received: 19 December 2023

Accepted: 14 August 2024

Published online: 18 September 2024

 Check for updates

Justine E. Paul<sup>1,2</sup>, Yuan Gao<sup>1,3,4,7</sup>, Yoo Kyung Go<sup>2,7</sup>, Luis E. Rodriguez Koett<sup>1,2,7</sup>, Anisha Sharma<sup>1,2</sup>, Manxin Chen<sup>1,3</sup>, Jacob J. Lessard<sup>1,5</sup>, Tolga Topkaya<sup>1,6</sup>, Cecilia Leal<sup>2</sup>, Jeffrey S. Moore<sup>1,5</sup>, Philippe H. Geubelle<sup>1,3</sup> & Nancy R. Sottos<sup>1,2✉</sup>

Materials with hierarchical architectures that combine soft and hard material domains with coalesced interfaces possess superior properties compared with their homogeneous counterparts<sup>1–4</sup>. These architectures in synthetic materials have been achieved through deterministic manufacturing strategies such as 3D printing, which require an a priori design and active intervention throughout the process to achieve architectures spanning multiple length scales<sup>5–9</sup>. Here we harness frontal polymerization spin mode dynamics to autonomously fabricate patterned crystalline domains in poly(cyclooctadiene) with multiscale organization. This rapid, dissipative processing method leads to the formation of amorphous and semi-crystalline domains emerging from the internal interfaces generated between the solid polymer and the propagating cure front. The size, spacing and arrangement of the domains are controlled by the interplay between the reaction kinetics, thermochemistry and boundary conditions. Small perturbations in the fabrication conditions reproducibly lead to remarkable changes in the patterned microstructure and the resulting strength, elastic modulus and toughness of the polymer. This ability to control mechanical properties and performance solely through the initial conditions and the mode of front propagation represents a marked advancement in the design and manufacturing of advanced multiscale materials.

Drawing inspiration from biological systems in which structural complexity develops through dissipative reaction–diffusion processes, this study explores a transformative synthetic manufacturing strategy aimed at harnessing the principles underpinning morphogenic growth, unlocking new avenues for advanced materials design and fabrication. Synthetic coupled reaction–transport processes offer a versatile yet relatively underexplored method to manipulate the spatial attributes of synthetic materials<sup>10</sup>. Here we introduce an innovative manufacturing approach based on frontal ring-opening metathesis polymerization (FROMP) that draws parallels with morphogenic growth and development, enabling the formation of patterned microstructures within polymeric materials.

Frontal polymerization is a thermally driven reaction–transport process in which a polymerization wave propagates through a monomer, transforming it into a polymer<sup>11–13</sup>. Stable front propagation in a uniform, planar configuration allows for rapid polymeric material production. Disruptions in the system, such as heat loss or variations in the initial composition, can destabilize this planar mode, resulting in pulsating, spinning and aperiodic front propagation<sup>11</sup>. Nonplanar spin modes have been studied for acrylate-based chemistries<sup>10,14–16</sup> and are characterized by the presence of one or more localized

high-temperature regions, that is, hot spots, which exhibit a helical or zigzag movement pattern dependent on the shape and the size of the reactor geometry<sup>17,18</sup>. This mode of propagation also introduces non-uniformities in the resulting polymer product<sup>19,20</sup>. More recently, pulsating and aperiodic front propagation was observed during FROMP of dicyclopentadiene (DCPD) and 1,5-cyclooctadiene (COD) in an open mould<sup>21</sup>. The unstable front propagation in DCPD led to surface pattern formation with spacing of the order of 10–100  $\mu\text{m}$ , but little change in material properties. Highly chaotic, irregularly shaped patterns with dimensions of the order of 1–3 cm were observed after FROMP of COD in an open mould. The patterns selectively crystallized in the resulting poly(cyclooctadiene) (pCOD), leading to variation in the elastic modulus across the polymer. Inspired by the temperature-responsive crystallization of pCOD achieved during FROMP in an open mould<sup>21</sup>, we proposed that by strategically harnessing nonplanar front propagation in a closed rectangular mould, unique polymer microstructures could be formed through a dissipative manufacturing process controlled by tuning the thermochemistry<sup>22</sup>, reaction kinetics and boundary conditions of the system (Fig. 1a).

Thermal FROMP of our initial formulation of COD with a Grubbs' second-generation catalyst (Ru-1) as the initiator and a phosphite

<sup>1</sup>Beckman Institute for Advanced Science and Technology, University of Illinois at Urbana–Champaign, Urbana, IL, USA. <sup>2</sup>Department of Materials Science and Engineering, University of Illinois at Urbana–Champaign, Urbana, IL, USA. <sup>3</sup>Department of Aerospace Engineering, University of Illinois at Urbana–Champaign, Urbana, IL, USA. <sup>4</sup>State Key Laboratory of Digital Manufacturing Equipment and Technology, School of Mechanical Science and Engineering, Huazhong University of Science and Technology, Wuhan, China. <sup>5</sup>Department of Chemistry, University of Illinois at Urbana–Champaign, Urbana, IL, USA. <sup>6</sup>Mechanical Engineering Department, Engineering and Architecture Faculty, Batman University, Batman, Turkey. <sup>7</sup>These authors contributed equally: Yuan Gao, Yoo Kyung Go, Luis E. Rodriguez Koett. ✉e-mail: n-sottos@illinois.edu

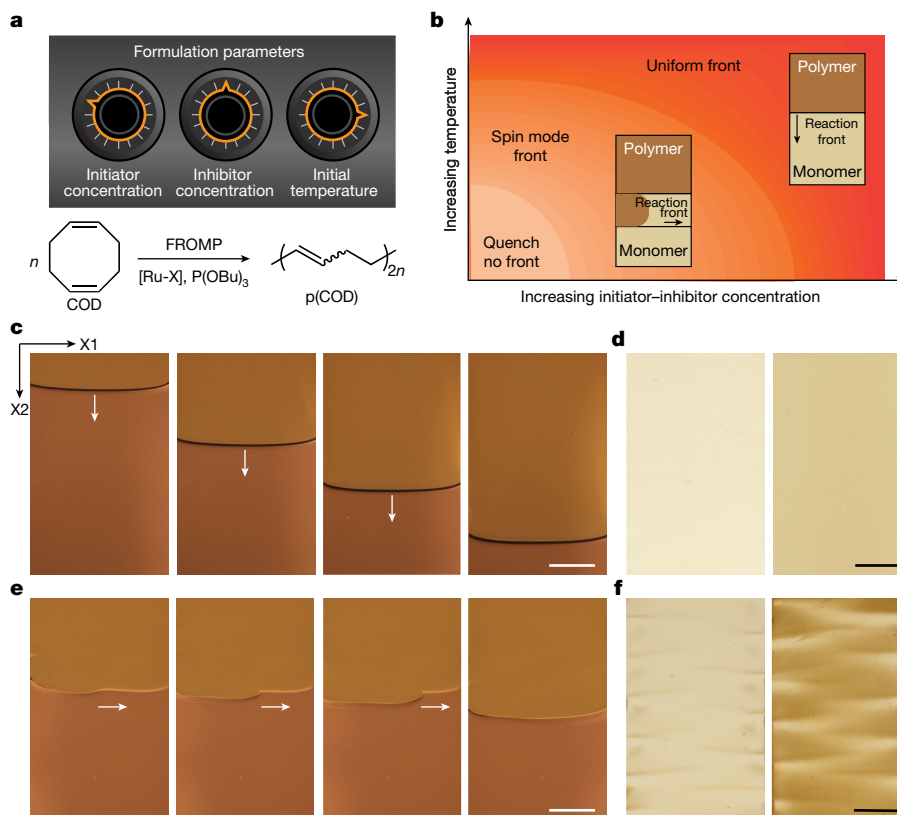


**Fig. 1 | Control of front dynamics.** **a**, Experimental knobs that control different modes (uniform and spin) of front propagation and the reaction scheme for the FROMP of COD by a thermally latent initiator (Ru-X) and an alkyl phosphite inhibitor (P(OBu<sub>3</sub>)). **b**, Schematic of the effects of increasing temperature and initiator–inhibitor concentration on the mode of front propagation for this system. **c**, Uniform mode of front propagation for the FROMP reaction of COD with Grubbs' second-generation ruthenium catalyst (Ru-1) and P(OBu<sub>3</sub>) (1.0 equiv. to the initiator). **d**, Representative optical images of pCOD specimen fabricated

by a uniform front after 2 h (left) and 24 h (right) post-polymerization. **e**, Spin mode of front propagation for the FROMP of COD with Ru-1 and P(OBu<sub>3</sub>) (2.0 equiv. to the initiator). **f**, Representative optical images of the patterned polymer fabricated by spin mode propagation after 2 h (left) and 24 h (right) post-polymerization. White arrows in **c** and **e** indicate the direction of the propagating reaction front. Scale bar, 5 mm (**c–f**). The gravity vector is in the direction of X2.

inhibitor (Fig. 1a) shows uniform front propagation in the X2 direction in a rectangular closed mould (Fig. 1c and Supplementary Video 1). Nonplanar front dynamics are triggered by small perturbations in reaction kinetics<sup>23</sup> and changes in ambient temperature. However, if the temperature is too low or the inhibitor concentration is too high, quenching of the propagating front or no frontal propagation is observed (Fig. 1b). Increasing the concentration of the phosphite inhibitor (from 1.0 equiv. to 2.0 equiv. to the initiator), while keeping all other conditions constant, resulted in the formation of fronts with highly regular spin modes that traverse back and forth in the X1 direction until complete conversion of monomer to polymer (Fig. 1e and Supplementary Video 2). This slight increase in inhibitor concentration results in a lower initiation rate for the spin mode formulation, indicated by a higher exothermic onset temperature observed in the dynamic cure profiles (Extended Data Fig. 1). The spin mode formulation also exhibits a marginally lower heat of reaction ( $H_r$ ), resulting in less heat diffusion to the monomer resin ahead of the front and greater heat loss to the surrounding environment (Extended Data Table 1).

This small difference in the resin formulation and associated front dynamics drives remarkable differences in time-dependent crystallization and the resulting structure of the final polymer product (Fig. 1d,f). Consistent with previous reports in the literature<sup>21,22</sup>, relatively homogeneous crystallization was observed in pCOD 24 h after frontal polymerization (Fig. 1d). By contrast, regularly spaced crystallization patterns emerged in spin mode samples consistent with the direction of the front propagation (Fig. 1f and Supplementary Video 3). The evolution of the polymer structure was characterized by nuclear magnetic

resonance (NMR), Raman spectroscopy and differential scanning calorimetry (Extended Data Fig. 2 and Supplementary Figs. 1–8). The *trans* content and the heat of fusion increased with time in both uniform and spin mode pCOD specimens. This evolution is attributed to the ruthenium initiator remaining active on the chain ends after frontal polymerization has completed, allowing for chain transfer events to occur post-polymerization<sup>24,25</sup>.

Our understanding of the thermochemistry, reaction kinetics, boundary conditions and initial selection of resin formulations was guided by numerical modelling of the front dynamics using the reaction–diffusion partial differential equations as shown in equation (1) (refs. 26,27) (Extended Data Fig. 3a and Extended Data Table 2). Two-dimensional finite-element simulations conducted using the Multiphysics Object-Oriented Simulation Environment (MOOSE) show that the spin mode of front propagation has two distinct thermal regions, a hot region (normalized maximum temperature,  $\theta_{\max} \approx 1.2$ ) and a cold region ( $\theta_{\max} \approx 0.8$ ), whereas the uniform mode of front propagation has only one distinct thermal region ( $\theta_{\max} \approx 1.0$ ). The uniform mode of front propagation was simulated with an initial ambient temperature of 35 °C, which minimizes the thermal diffusion to the immediate surroundings, whereas the spin mode of front propagation was simulated at 25 °C. Figure 2a shows the simulated evolution of temperature ( $T$ ) and degree of cure ( $\alpha$ ) at the three distinct thermal regions during the polymerization processes: uniform mode (grey curve), spin mode hot region (red curve) and spin mode cold region (blue curve). The contour of reaction rates (dotted lines) for each mode of propagation was derived from the cure kinetic model and fit with the experimental data

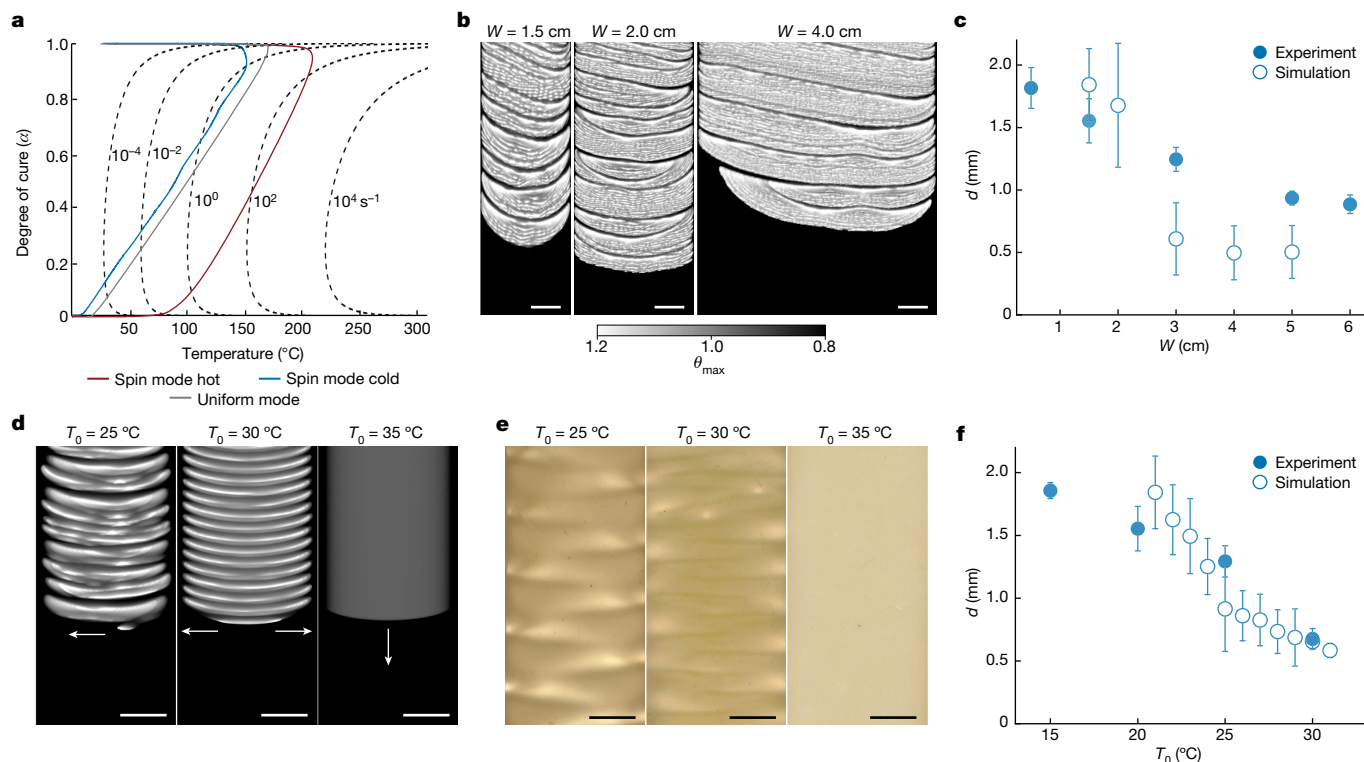


**Fig. 2 | Spatially controlled material domains.** **a**, Computed evolution of the degree of cure ( $\alpha$ ) with temperature for spin mode front propagation and uniform mode front propagation for COD with Ru-1. The reaction rate is determined by cure kinetics,  $d\alpha/dt$  (dotted lines, with units  $s^{-1}$ ), as a function of the temperature and  $\alpha$ . **b**, Snapshots of nonplanar front dynamics observed in simulations for varying widths ( $W$ ) of the mould (1.5 cm, 2.0 cm and 4.0 cm).  $\theta_{\max} = (T_{\max} - T_0)/(H_r/C_p)$  is the normalized maximum temperature, where  $T_{\max}$ ,  $T_0$ ,  $H_r$  and  $C_p$  denote the maximum and initial temperatures, heat of reaction and specific heat capacity, respectively. **c**, Average spacing between material domains ( $d$ ) as a function of the width of the closed mould for COD with Ru-1. The ambient temperature was held constant at 20 °C for all specimens. **d**, Computed thermal profiles of the spin mode of front propagation at

(Extended Data Fig. 3b). The slope of the line for the uniform mode is approximately equal to the heat of reaction  $H_r$  divided by the specific heat capacity of the resin ( $C_{p,r}$ ), implying that the time scale of the reaction is faster than the heat that is dissipated to the surroundings, thus resulting in the uniform mode of front propagation. The spin mode of front propagation necessitates a higher energy input to trigger the reaction because of a lower initial temperature. Meanwhile, the heat loss at the boundaries is more pronounced than that of the uniform mode, leading to a more heterogeneous spatial temperature distribution. The hot region accumulates more heat before the polymerization is kicked off, and the reaction rate accelerates, reaching approximately  $10^2 s^{-1}$ . The slope of  $(d\alpha/dT)$  for the spin mode hot region is slightly greater than that of the uniform mode as it forms into a polymer more rapidly and then diffuses the heat from the reaction to the cold regions, continuing the polymerization process. The spin mode cold region receives less heat before polymerization is kicked off, resulting in lower reaction rates than the hot region. The discrepancy in reaction rates between the hot and cold regions contributes to the formation of the observed spin modes, which are evident in both experimental observations and simulations.

Systematic experimental and numerical studies show that the boundary conditions of the system control the size and spacing ( $d$ ) of the crystalline domains<sup>28</sup>. Consistent with previous reports for acrylates<sup>17,18</sup>, an increase in specimen width leads to a greater amount of heat generated per unit surface area, accelerated propagation of the spin mode

different initial temperatures (25 °C, 30 °C and 35 °C). The white arrows signify the direction of the propagating fronts. **e**, Representative optical images of the resulting patterned specimens 24 h post-polymerization. Specimens were fabricated at various ambient temperatures using COD and the Ru-1 initiator. The width of the mould for **d** and **e** was held constant at 1.5 cm. **f**, Average spacing between material domains ( $d$ ) as a function of the ambient temperature. In **c** and **f**, the experimental results are represented by filled blue circles and simulated results are represented by open blue circles. Experimental error bars represent the maximum and minimum values ( $n = 3$ ) and error bars of the simulated data result from averaging the spacing value during the front propagation of 4 cm for each case. Scale bars, 5 mm (**b,d,e**).

and a decrease in domain spacing (Fig. 2b,c and Supplementary Fig. 12). Multi-head spin modes were observed in both experiments and simulations for wider rectangular specimen geometries ( $W > 2$  cm) and in cylindrical moulds (Supplementary Videos 4, 5 and 7). Increasing the ambient temperature from 25 °C to 30 °C results in enhanced reaction kinetics, an accelerated spin mode of front propagation and a consequent decrease in the predicted and observed spacing between material domains with the Ru-1 initiator (Fig. 2d–f). Increasing the temperature to 35 °C results in the loss of the spin mode and return to the uniform mode of front propagation. This result is attributed to the predominance of the thermochemistry and reaction rate over the thermal transport to the surroundings of the system. Conversely, when the ambient temperature is lowered below 15 °C, the reaction rate is notably suppressed and the heat loss is enhanced, resulting in front quenching. Numerical simulations consistently predict the experimental trends in material domain spacing and provide a powerful tool for predicting the necessary conditions to produce a desired patterned semi-crystalline material (Supplementary Table 4).

Comparative analysis of small- and wide-angle X-ray scattering patterns of both uniform and patterned polymers showed notable distinctions in lamellae alignment, with a length scale linked to the propagating front (micrometres), and polymer chain alignment on a sub-nanometre scale in the X2 scan direction (Fig. 3a and Supplementary Fig. 9). These findings are consistent with the previous investigations of crystallization in non-FROMP systems<sup>29–32</sup>. The shear flow

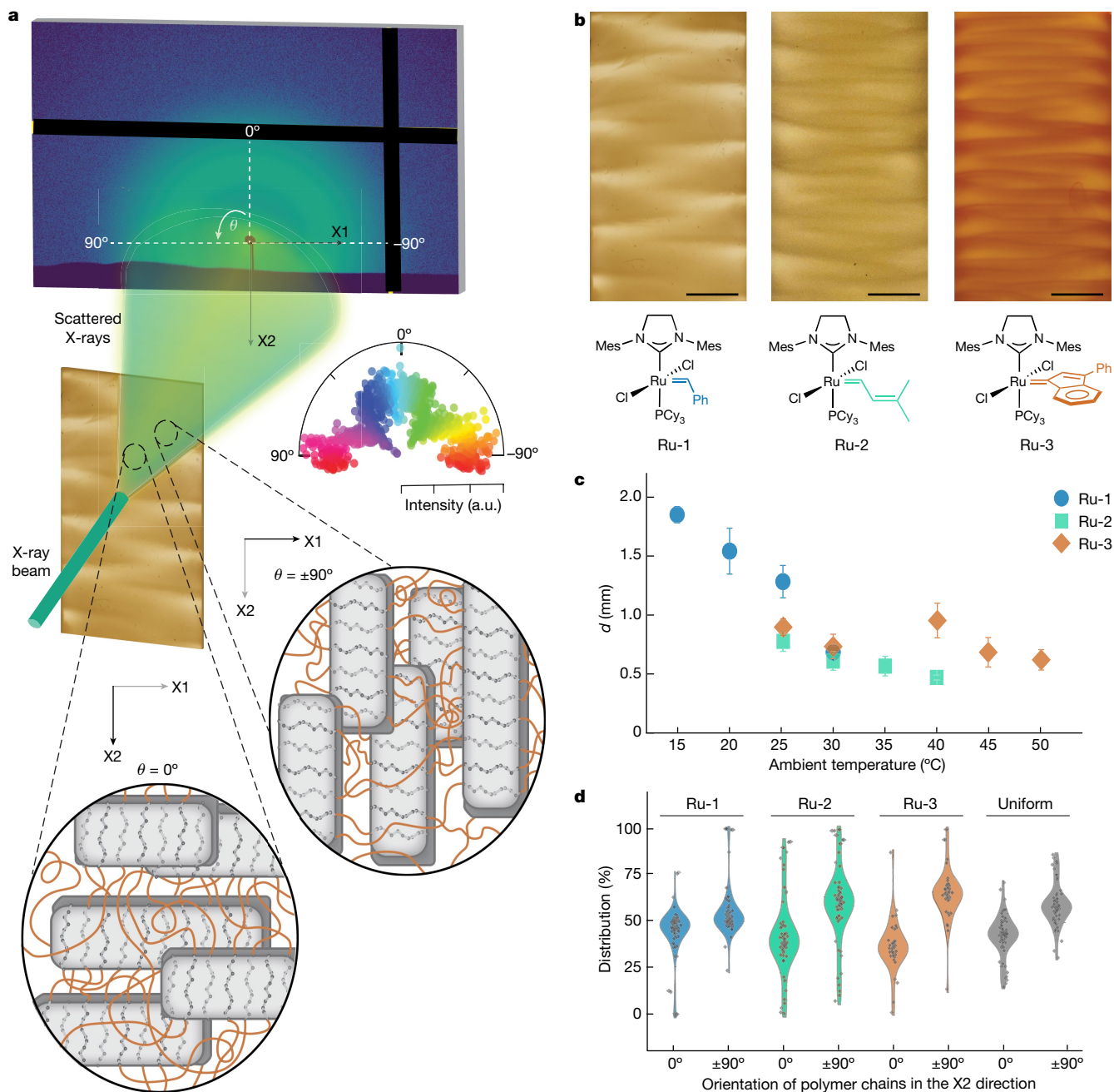


**Fig. 3 | Characterization of material microstructure and domains. a**, Small-angle X-ray scattering pattern obtained for both the patterned and uniform specimens (top). Small- and wide-angle X-ray scattering patterns were collected for a 20-mm line scan along the X2 direction. Data were collected every 0.25 mm. The azimuthal profile of the lamellae diffraction pattern highlights the distribution of preferred polymer chain orientations (middle). Illustration of the lamellae and polymer chain orientations observed in the X2 direction (line scan direction) for both the patterned and uniform specimens (bottom). **b**, Representative optical images, taken 24 h post-polymerization, of the

induced in the monomer by hot and cold spin mode regions during front propagation substantially affected the growth direction within the semi-crystalline domains<sup>33</sup>. Azimuthal integrations along the X2 out-of-plane direction provide quantitative insights into the orientation of the polymer chains and lamellae at angles of  $\theta = 0^\circ$  and  $\theta = \pm 90^\circ$  and the intricate relationships between the polymer morphology, alignment and properties of the polymers (Extended Data Fig. 4 and Supplementary Fig. 10). Small- and wide-angle X-ray scattering data suggest that the polymer chains preferentially align orthogonally to

the lamellae orientation but with a distribution of chain alignment angles observed. Small perturbations in the initial resin formulation lead to controlled changes in the final architecture of the polymer. Tuning of the resin formulation through the choice of ruthenium initiator and inhibitor concentration enables the manipulation of the macro- and micro-scale domain architectures. A single ligand difference between the initiators (Ru-1, Ru-2 or Ru-3) (ref. 34) alters the initiation kinetics (Extended Data Fig. 1b) and results in notable changes in the size and spacing

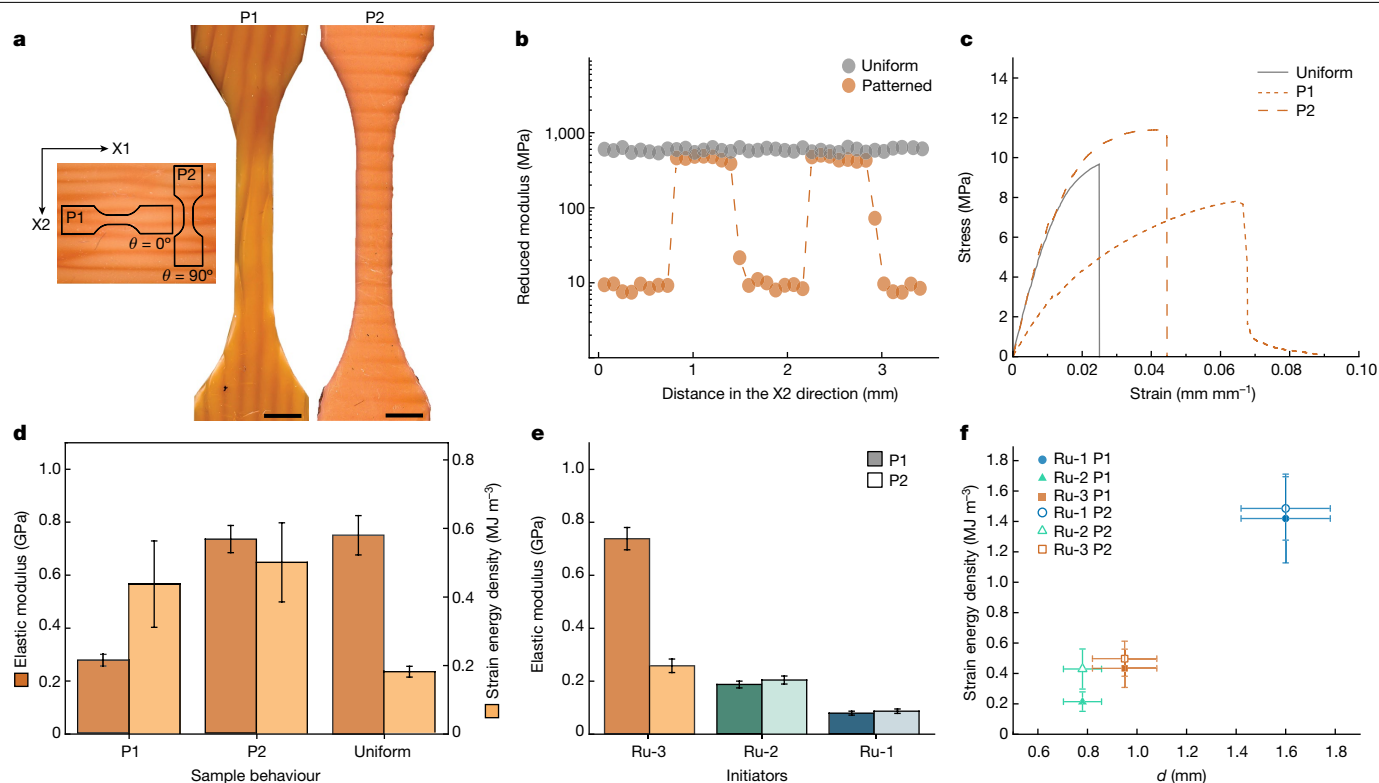


**Fig. 4 | Tunable mechanical response.** **a**, Schematic (left) showing the two directions the uniaxial tensile specimens were extracted. Representative tensile specimens were fabricated using the Ru-3 initiator for both the P1 (middle) and P2 (right) test directions. Images were enhanced for better clarity. Scale bars, 3 mm. **b**, Reduced modulus as a function of distance in the X2 direction obtained by nanoindentation for both a uniform and a patterned 1.5-cm-wide specimen fabricated with the Ru-3 initiator 24 h post-polymerization. **c**, Representative stress–strain curves from uniaxial tensile measurements of both uniform and

patterned specimens fabricated using the Ru-3 initiator. **d**, Elastic modulus and strain energy density for patterned and uniform specimens polymerized with the Ru-3 initiator. **e**, Elastic modulus of patterned specimens polymerized using Ru-1, Ru-2 and Ru-3 initiators for both the P1 and P2 specimens. **f**, Comparison of the strain energy density for patterned specimens fabricated using three different ruthenium initiators (Ru-1, Ru-2 and Ru-3) in both the P1 and P2 test directions as a function of domain spacing. Error bars in **d**, **e** and **f** represent the 95% confidence intervals from the mean ( $n = 5$ ).

of the polymer semi-crystalline domains (Fig. 3b–d). Owing to the differences in the initiation kinetics of the three resin formulations, the relative amount of inhibitor for Ru-2 and Ru-3 must be decreased to obtain successful spin mode propagation (Extended Data Table 1). Alternatively, adjusting the initiator concentration or modifying the ambient temperature enables us to induce spin modes in these formulations initiated by either heat or light (Supplementary Videos 6 and 7).

Comparison of the structure of polymers made with the three different initiators shows reproducible variations in the orientation of the polymer chains with respect to the X2 direction (Fig. 3d). This diversity in chain orientation provides an additional dimension of control for final material properties. Among the three initiators, Ru-3 exhibited the largest anisotropy in the percentage distribution of chains orientated at  $0^\circ$  versus those orientated at  $90^\circ$  (Extended Data Table 3). Even in uniform specimens, a discernible preference for polymer chain orientation was observed, indicating that planar fronts propagating in the X2 direction exert an influence on the alignment of the polymer chains within the material. The spatial distribution and alignment of these chains, alongside the packing of lamellae within the patterned materials, affect the resulting mechanical properties as compared with the uniform counterparts.

The preferential orientation of polymer semi-crystalline domains has a profound impact on the heat transport and optical properties of polymeric materials<sup>35</sup>. To understand how the mechanical properties are affected by the dynamics of the nonplanar front and the orientations of the polymer chains and lamellae, we prepared tensile coupons with domains orientated along the P1 ( $\theta = 0^\circ$ ) and P2 ( $\theta = 90^\circ$ ) directions (Fig. 4a). The local variation in properties along the length of

the specimen was characterized by nanoindentation. The presence of frontal polymerization spin modes led to the formation of the material domains with a two-fold difference in the reduced modulus along the X2 direction 24 h post-polymerization. By contrast, specimens generated through the uniform mode of front propagation did not exhibit any deviations in the resultant material characteristics (Fig. 4b, Extended Data Fig. 5 and Supplementary Fig. 14).

The anisotropy of patterned materials fabricated using the Ru-3 initiator leads to concurrent increases in elastic modulus, tensile strength and toughness in the P2 loading direction when compared with the P1 direction and the Ru-3 uniform specimens (Fig. 4c,d, Extended Data Fig. 5c and Extended Data Table 4). The Ru-3 P2 patterned specimen has 18% higher tensile strength and a 178% higher strain energy density (area under stress–strain curve) than the uniform specimen. The presence of hard and soft material domains in P2 leads to a significant increase in strain to failure and toughness, with little change in elastic modulus (730 MPa). P1 specimens have even higher strain to failure, but this ductile failure is accompanied by lower elastic modulus (about 275 MPa) and tensile strength (7.6 MPa). We attribute the distinctive anisotropic characteristics observed in the Ru-3 patterned specimens to the greater percentage distribution of polymer chains orientated  $90^\circ$  to the loading direction of the P2 specimens (Fig. 3d).

We also compared the properties of the patterned and uniform FROMP materials with the Ru-3 specimens subjected to oven curing by ROMP (Supplementary Figs. 15 and 16). The patterned FROMP samples had higher strain energy density than samples with similar formulation produced by ROMP (Extended Data Table 4), and the tensile behaviour

of the ROMP samples was not as anisotropic (similar tensile response in the P1 and P2 directions).

The tensile properties and associated toughness of the patterned materials depend on several complex factors, including the size, spacing and orientation of the larger crystalline domains, as well as the orientation of the polymer chains within the crystalline region<sup>36</sup>. The changes in polymer orientation and domain spacing created by the frontal spin modes for resin formulations with different initiators (Ru-1, Ru-2 and Ru-3) and ambient processing temperatures (Fig. 3b–d) had a marked effect on the tensile properties and toughness of the patterned polymers. Ru-3 patterned polymers were the most anisotropic and had the highest modulus in the P2 direction (Fig. 4e). By contrast, Ru-1 patterned polymers exhibited a significantly lower modulus and much less anisotropy. This difference in anisotropy and elastic modulus closely correlates with the preferred orientation of polymer chains in each system (Fig. 3d and Extended Data Table 3). Even more significant is the correlation between domain spacing and strain energy density summarized in Fig. 4f. Ru-1 patterned polymers had the highest strain energy density associated with the largest domain size. Overall we see a trend of increasing ductility (higher strain energy density) with increasing domain size. We further propose that substantial internal interpenetration of amorphous chains occurs within the semi-crystalline regions leading to enhanced toughness for certain orientations of the patterned specimen. We observe considerable fibril formation and ductile failure in the patterned samples (Supplementary Videos 8–10) in contrast to the brittle failure of uniform specimens, corroborated by the fracture surfaces shown in Supplementary Fig. 17.

In summary, polymers with patterned crystalline domains were manufactured by harnessing the nonplanar spin modes that arise during frontal polymerization. In contrast to conventional additive manufacturing that relies on deterministic, preprogrammed structure, this new methodology leverages dissipative reaction–diffusion processes to create polymers with patterned microstructures and tunable material properties. Guided by numerical simulations, deliberate selection of resin formulation and boundary conditions led to precise control over the spacing of the resulting material domains (amorphous and semi-crystalline). Increases in ambient temperature and specimen geometry led to a decrease in material domain size. A single ligand difference between the three initiators (Ru-1, Ru-2 and Ru-3) led to changes in reaction kinetics and the spin mode dynamics, also resulting in changes in the domain size of the material. In turn, the domain size had a marked impact on mechanical properties. Ru-1 patterned polymers with larger domain sizes had significantly higher ductility and toughness. Furthermore, we measured variations in the orientation of polymer chains and lamellae that substantially influenced the material properties of the patterned materials generated by the three initiators. Ru-3 patterned polymers with enhanced chain orientation in the  $\pm 90^\circ$  direction exhibited significant anisotropy and enhanced toughness in comparison with their uniform counterparts. The control of architecture and toughness achieved through spin mode front propagation in semi-crystalline polymers represents an entirely new pathway for enhancing material resilience and functionality solely through initial resin formulation and boundary conditions. Given the relatively large library of unexplored monomers capable of frontal polymerization, dissipative processing methods offer an opportunity to control polymer properties and unique advantages with respect to resolution and performance over more deterministic additive manufacturing platforms.

## Online content

Any methods, additional references, Nature Portfolio reporting summaries, source data, extended data, supplementary information, acknowledgements, peer review information; details of author contributions and competing interests; and statements of data and code availability are available at <https://doi.org/10.1038/s41586-024-07951-7>.

- Aizenberg, J. et al. Skeleton of *Euplectella* sp.: structural hierarchy from the nanoscale to the macroscale. *Science* **309**, 275–278 (2005).
- Deville, S., Saiz, E., Nalla, R. K. & Tomsia, A. P. Freezing as a path to build complex composites. *Science* **311**, 515–518 (2006).
- Huang, W. et al. Multiscale toughening mechanisms in biological materials and bioinspired designs. *Adv. Mater.* **31**, 1901561 (2019).
- Rylski, A. K. et al. Polymeric multimaterials by photochemical patterning of crystallinity. *Science* **378**, 211–215 (2022).
- Truby, R. L. & Lewis, J. A. Printing soft matter in three dimensions. *Nature* **540**, 371–378 (2016).
- Larson, N. M. et al. Rotational multimaterial printing of filaments with subvoxel control. *Nature* **613**, 682–688 (2023).
- Raney, J. R. et al. Rotational 3D printing of damage-tolerant composites with programmable mechanics. *Proc. Natl Acad. Sci. USA* **115**, 1198–1203 (2018).
- Lei, M., Hamel, C. M., Yuan, C., Lu, H. & Qi, J. H. 3D printed two-dimensional periodic structures with tailored in-plane dynamic responses and fracture behaviors. *Compos. Sci. Technol.* **159**, 189–198 (2018).
- Esmaili, M. et al. 3D printing-assisted self-assembly to bio-inspired Bouligand nanostructures. *Small* **19**, 2206847 (2023).
- Epstein, I. R. & Pojman, J. A. *An Introduction to Nonlinear Chemical Dynamics: Oscillations, Waves, Patterns, and Chaos* (Oxford Academic, 1998).
- Suslick, B. A. et al. Frontal polymerizations: from chemical perspectives to macroscopic properties and applications. *Chem. Rev.* **123**, 3237–3298 (2023).
- Robertson, I. D. et al. Rapid energy-efficient manufacturing of polymers and composites via frontal polymerization. *Nature* **557**, 223–227 (2018).
- Pojman, J. A. in *Polymer Science: A Comprehensive Reference* Vol. 4 (eds Matyjaszewski, K. & Möller, M.) 957–980 (Elsevier, 2012).
- Ilyashenko, V. M. & Pojman, J. A. Single-head spin modes in frontal polymerization. *Chaos* **8**, 285–289 (1998).
- Pojman, J. A., Ilyashenko, V. M. & Khan, A. M. Spin mode-instabilities in propagating fronts of polymerization. *Phys. D Nonlinear Phenom.* **84**, 260–268 (1995).
- Huh, D. S. & Kim, H. S. Bistability of propagating front with spin-mode in a frontal polymerization of trimethylpropane triacrylate. *Polym. Int.* **52**, 1900–1904 (2003).
- Masere, J., Stewart, F., Meehan, T. & Pojman, J. A. Period-doubling behavior in frontal polymerization of multifunctional acrylates. *Chaos* **9**, 315–322 (1999).
- Pojman, J. A. et al. The effect of reactor geometry on frontal polymerization spin modes. *Chaos* **12**, 56–65 (2002).
- Mahji, S. S., Yadav, N. & Chakraborty, A. K. Development of periodic colored bands via frontal polymerization. *J. Ind. Chem. Soc.* **99**, 100721 (2022).
- Lessard, J. J. et al. Switching frontal polymerization mechanisms: FROMP and Frap. *ACS Macro Lett.* **11**, 1097–1101 (2022).
- Lloyd, E. M. et al. Spontaneous patterning during frontal polymerization. *ACS Cent. Sci.* **7**, 603–612 (2021).
- Dean, L. M., Wu, Q., Alshangiti, O., Moore, J. S. & Sottos, N. R. Rapid synthesis of elastomers and thermosets with tunable thermomechanical properties. *ACS Macro Lett.* **9**, 819–824 (2020).
- Solovoyov, S. E., Ilyashenko, V. M. & Pojman, J. A. Numerical modeling of self-propagating polymerization fronts: the role of kinetics on front stability. *Chaos* **7**, 331–340 (1997).
- Alzate-Sanchez, D. M. et al. Rapid controlled synthesis of large polymers by frontal ring-opening metathesis polymerization. *Macromolecules* **56**, 1527–1533 (2023).
- Lenz, R. W., Ohata, K. & Funt, J. Crystallization-induced reactions of copolymers. II. *Cis-trans* isomerization of 1,4-poly-1,3-butadiene. *J. Polym. Sci.* **11**, 2273–2285 (1973).
- Goli, E., Robertson, I. D., Geubelle, P. H. & Moore, J. S. Frontal polymerization of dicyclopentadiene: a numerical study. *J. Phys. Chem. B* **122**, 4583–4591 (2018).
- Pojman, J. A. Mathematical modeling of frontal polymerization. *Math. Model. Nat. Phenom.* **14**, 604 (2019).
- Goli, E., Gai, T. & Geubelle, P. H. Impact of boundary heat losses on frontal polymerization. *J. Phys. Chem. B* **124**, 6404–6411 (2020).
- Gbabode, G. et al. Unique crystal orientation of poly(ethylene oxide) thin films by crystallization using a thermal gradient. *Macromolecules* **50**, 5877–5891 (2017).
- Suehiro, K. & Takayanagi, M. Structural studies of the high temperature form of trans-1,4-polybutadiene crystal. *J. Macromol. Sci. B* **4**, 39–46 (1970).
- Viglid, M. E., Chu, C., Sugiyama, M., Chaffin, K. A. & Bates, F. S. Influence of shear on the alignment of a lamellae-forming pentablock Copolymer. *Macromolecules* **34**, 951–964 (2001).
- Mitchell, G. R. et al. Controlling and evaluating the structure and morphology of polymers on multiple scales. *J. Mater. Sci. Chem. Eng.* **3**, 48–60 (2015).
- Chen, W., Zhang, Q., Zhao, J. & Li, L. Molecular and thermodynamic descriptions of flow induced crystallization in semi-crystalline polymers. *J. Appl. Phys.* **127**, 241101 (2020).
- Suslick, B. A., Stawiasz, K., Sottos, K. J., Paul, J. E., Sottos, N. R. & Moore, J. S. Survey of catalysts for frontal ring-opening metathesis polymerization. *Macromolecules* **54**, 5117–5123 (2021).
- Shin, J. et al. Light-triggered thermal conductivity switching in azobenzene polymers. *Proc. Natl Acad. Sci. USA* **116**, 5973–5978 (2019).
- Yu, L. & Christie, G. Microstructure and mechanical properties of orientated thermoplastic starches. *J. Mater. Sci.* **40**, 111–116 (2005).

**Publisher's note** Springer Nature remains neutral with regard to jurisdictional claims in published maps and institutional affiliations.

Springer Nature or its licensor (e.g. a society or other partner) holds exclusive rights to this article under a publishing agreement with the author(s) or other rightsholder(s); author self-archiving of the accepted manuscript version of this article is solely governed by the terms of such publishing agreement and applicable law.

© The Author(s), under exclusive licence to Springer Nature Limited 2024

## Methods

### Materials

COD and tributyl phosphite were purchased from TCI America. COD was passed through a plug of basic alumina to remove the octadecyl 3-(3',5'-di-tert-butyl-4'-hydroxyphenyl) propionate stabilizer. Tributyl phosphite was stored under an inert atmosphere. 5-Ethylidene-2-norbornene (ENB), Grubbs' Catalyst M204 (Ru-1), Grubbs' Catalyst M207 (Ru-2) and Grubbs' Catalyst M202 (Ru-3) were purchased from Sigma-Aldrich and used as received. A 26-gauge Kanthal wire ( $D = 0.40$  mm, resistivity  $= 1.4 \times 10^{-4}$   $\Omega$  cm) was used to initiate FROMP. High-temperature silicone rubber gaskets were purchased from McMaster-Carr. Glass slides of 1 mm thickness were purchased from Ted Pella.

### Frontal polymerization

In a typical experiment for the spin mode of front propagation with the Ru-1 initiator, 5.29 g (6 ml, 5,400 mol equiv. to Ru-1) of monomer resin composed of 97 wt% COD (5.13 g/5.82 ml) and 3 wt% ENB (0.16 g/0.18 ml) was measured out in a vial. Unless otherwise noted, all references to COD refer to the 97:3 COD/ENB mixture. The phosphite inhibitor (4.98  $\mu$ l, 0.0184 mmol, 2 mol equiv. to Ru-1) was then added to the vial with monomer using a microlitre syringe. In a separate vial, 7.68 mg (0.00905 mmol) of the Ru-1 initiator was weighed out. The monomer-inhibitor solution was then added to the vial containing the initiator, and the resulting mixture was sonicated for 5 min to ensure complete dissolution of the initiator. The monomer resin was then added to a rectilinear geometry before the initiation of the front. Please refer to Extended Data Table 1 for the other resin formulations that yielded uniform and spin modes of front propagation with Ru-1, Ru-2 and Ru-3 initiators. Rectilinear closed moulds were fabricated by compressing a U-shaped high-temperature silicone rubber gasket cut into the desired geometry between two 1-mm thick glass slides. For a typical experiment, the frontal polymerization process was carried out in a 1.5 cm  $\times$  6.0 cm ( $w \times h$ ) geometry with a 5-mm thick silicone rubber gasket. The polymerization was initiated by local heating with a 26-gauge resistive wire and an Agilent (U8031A) triple-output programmable d.c. power supply (3.5 V, 3.0 A). The ambient temperature was maintained in a custom-built environmental chamber equipped with an AC-162 Peltier module, TC-720 temperature controller and PS-2425 power supply from TE Technology. Target ambient temperature  $T_0$  was achieved by setting the environmental chamber to the desired temperature and monitoring with a thermocouple. A schematic of the mould and initiation scheme used for experiments is shown in Extended Data Fig. 1a.

### Front velocity and temperature measurements

To a 13 mm  $\times$  100 mm test tube, 8 ml of freshly prepared monomer mixture was immediately transferred. FROMP was initiated from the top of the test tube using the tip of a soldering iron, set to the highest heat setting. The front propagation is tracked with a Canon EOS R5 DSLR camera. Frontal velocities were measured using Tracker, an open-source physics video analysis and modelling tool. Using the built-in tracking feature, position, time and velocity were extracted from the videos. Each video was analysed thrice, and the front velocity of the resin formulation was determined by the average of the three samples. To measure the maximum front temperature, a T-type thermocouple (TMQSS, Omega) was inserted at the centre of the test tube before initiating FROMP and the temperature profiles were monitored by a custom Labview program. The average maximum front temperature was taken from an  $n = 3$ .

### Heat of reaction and heat of fusion analysis

Differential scanning calorimetry (DSC) measurements were carried out on a TA Instruments Discovery DSC 250 equipped with an

RCS 90 cooling system and an autosampler. Samples were transferred into aluminium hermetic DSC pans at room temperature and sealed. The sample mass was determined using an analytical balance (XPE205, Mettler Toledo). The mass of the liquid resin samples was carefully maintained to ensure the maximum heat flow of the exothermic reaction was between 6 mW and 10 mW. Dynamic curing profiles of liquid resins were determined at temperatures between  $-50$   $^{\circ}$ C and  $180$   $^{\circ}$ C with constant ramp rates (Extended Data Fig. 1b). The heat of reaction ( $H_r$ ) was determined through the integration of heat flow over the exothermic peak after baseline correction for cure profiles<sup>37</sup> with a ramp rate of  $5$   $^{\circ}$ C  $\text{min}^{-1}$ . The heat of fusion ( $H_f$ ) was measured by cutting cured polymer specimens at various time points and transferring them into aluminium hermetic DSC pans at room temperature. The mass of the polymer specimens was carefully maintained between 5 mg and 10 mg. The melting profiles of polymer specimens were determined at temperatures between  $20$   $^{\circ}$ C and  $150$   $^{\circ}$ C with a constant ramp rate of  $10$   $^{\circ}$ C  $\text{min}^{-1}$ . The endothermic peak in the heat flow signal was integrated to extract the heat of fusion for each specimen.

### Nanoindentation

Nanoindentation was performed with a Hysitron TI-950 TriboIndenter equipped with a Hysitron 3D Ominprobe high-load transducer and Berkovich tip from Bruker. Samples that were left to sit for 24 h post-polymerization at room temperature were loaded at  $0.2$   $\text{mN s}^{-1}$  up to a maximum load of 8 mN, which was held for 5 s, and subsequently unloaded at  $0.2$   $\text{mN s}^{-1}$ . Reduced moduli were calculated from the unloading curves using the Hysitron software by fitting a slope to the unloading force-displacement curve.

### Raman confocal imaging

Raman spectra were obtained with a Horiba LabRAM HR 3D Raman confocal imaging microscope equipped with an 830-nm laser, a 300 groove  $1$   $\text{mm}^{-1}$  grating (blazed at 600 nm), a long working distance  $20\times$  objective from Leica and a Horiba Synapse back-illuminated deep depletion CCD camera<sup>38</sup>.

### Nuclear magnetic resonance

$^1\text{H}$  NMR and  $^{13}\text{C}$  spectra were obtained at room temperature in deuterated chloroform ( $\text{CDCl}_3$ ) on Bruker CB500 with cryoprobe ( $^1\text{H}$  NMR at 500 MHz and  $^{13}\text{C}$  NMR at 126 MHz), using deuterium lock. Data for  $^1\text{H}$  NMR spectra are quoted relative to solvent as an internal standard (7.26 ppm), and data for  $^{13}\text{C}$  NMR spectra are quoted relative to dichloromethane as an internal standard (77.16 ppm).  $^1\text{H}$  NMR spectra were collected over 16 scans from 16 ppm to  $-4$  ppm.  $^{13}\text{C}$  NMR spectra were collected over 252 scans from 235 ppm to  $-15$  ppm. Heteronuclear single quantum coherence (HSQC) NMR spectra were collected over the range used in the one-dimensional NMR studies.

### Computational modelling

Numerical analyses were conducted in a two-dimensional domain comprising two subdomains of the COD resin and the silicone rubber bands, as presented in Extended Data Fig. 1. The length ( $l = 50$  mm) and width ( $W_s = 2.5$  mm) of the silicone rubber band were kept as constant in all simulations, whereas the width of the COD resin  $w$ , varied between 5 mm and 50 mm, consistent with the experimental setup. The polymerization front was numerically initiated at an inclined boundary (marked by the red dashed line) to mimic the asymmetric effect on frontal polymerization in the experiment. The length of the boundaries  $l_1 = 2$  mm and  $l_2 = 1$  mm remained constant in all simulations. The glass mould was not explicitly considered in the numerical analyses.

Frontal polymerization of COD was modelled by the following reaction-diffusion partial differential equations:

$$\begin{cases} \kappa_r \nabla^2 T + \rho_r H_r \frac{\partial \alpha}{\partial t} - H(T - T_0) = \rho_r C_{p,r} \frac{\partial T}{\partial t}, \\ \frac{\partial \alpha}{\partial t} = A \exp\left(-\frac{E}{RT}\right) g(\alpha). \end{cases} \quad (1)$$

The main variables are the temperature  $T$  (in K) and the degree of cure  $\alpha$  (dimensionless), which takes values between 0 (monomer) and 1 (polymer) and describes the fractional conversion based on the enthalpy of the reaction. In the first equation,  $\kappa_r$  (in  $\text{W mK}^{-1}$ ),  $\rho_r$  (in  $\text{kg m}^{-3}$ ),  $H_r$  (in  $\text{J kg}^{-1}$ ), and  $C_{p,r}$  (in  $\text{J kg}^{-1} \text{K}^{-1}$ ) represent the thermal conductivity, density, enthalpy of reaction and heat capacity of the resin, respectively, with the subscript 'r' denoting the resin. The term  $-H(T - T_0)$  was introduced to approximate the heat loss through the glass mould, where  $H = 140 \text{ kW m}^{-3}$  is the heat loss coefficient. With this setting, a quenched front was observed with  $W = 5 \text{ mm}$  at room temperature, consistent with experimental observation. The second equation models the cure kinetics of the resin, where  $A$  (in  $\text{s}^{-1}$ ),  $E$  (in  $\text{J mol}^{-1}$ ),  $R$  ( $=8.314 \text{ J kg}^{-1} \text{K}^{-1}$ ) represent the pre-exponential factor, activation energy and the ideal gas constant, respectively. The Prout–Tompkins model<sup>39</sup> was adopted to capture the dependence of cure kinetics on  $\alpha$ , and  $g(\alpha) = (1 - \alpha)^n \alpha^m$ , where  $n$  (dimensionless) and  $m$  (dimensionless) are reaction orders. The thermal conduction in the silicone rubber (subscript 's') was modelled by

$$\kappa_s \nabla^2 T - H(T - T_0) = \rho_s C_{p,s} \frac{\partial T}{\partial t}. \quad (2)$$

A Dirichlet boundary condition  $T(x, y, t) = 160 \text{ }^\circ\text{C}$  was adopted at the inclined boundary for  $t \leq 5 \text{ s}$  to trigger the polymerization front, and an adiabatic boundary condition was imposed to replace the Dirichlet boundary condition. Adiabatic boundary conditions were used at all other boundaries. The continuity of temperature and heat flux were imposed at all material interfaces between the COD resin and the silicone rubber bands. The initial degree of cure  $\alpha_0$  was set as 0.04 and the initial temperature varied between  $20 \text{ }^\circ\text{C}$  and  $40 \text{ }^\circ\text{C}$ .

The thermal properties of COD and silicone rubber are adopted from literature<sup>21,40</sup> and given in Extended Data Table 2. DSC tests were performed under various temperature ramping rates to parametrize  $H_r$ ,  $A$ ,  $E$ ,  $n$  and  $m$ . The cure kinetics parameters are presented in Extended Data Table 2, and the comparison between the DSC experiments and cure kinetics model is demonstrated in Extended Data Fig. 2. The cure kinetics model can be further validated by comparing the numerical front velocity of  $0.44 \text{ mm s}^{-1}$  and front temperature of  $162.7 \text{ }^\circ\text{C}$  in unidirectional frontal polymerization with the experimental values of  $0.45 \text{ mm s}^{-1}$  and  $159.2 \text{ }^\circ\text{C}$  measured in the frontal polymerization experiments in a test tube.

All finite-element simulations were conducted using the Multiphysics Object-Oriented Simulation Environment (MOOSE)<sup>41</sup>, an open-source C++ finite-element solver with robust mesh and time-step adaptivity to capture the gradients in temperature and degree of cure in the vicinity of the unstable polymerization front. The average size of the mesh was about  $0.4 \text{ mm}$ , and the h-level of the mesh adaptivity was set as 6. The typical time step was  $0.01 \text{ s}$  and was reduced to around  $0.00001 \text{ s}$  when experiencing large gradients of  $T$  and  $\alpha$  during instabilities.

### Image analysis

Optical images of the resulting polymer specimens 24 h post-polymerization were captured using a digital microscope (VHX-5000, Keyence) with a  $20\times$  objective. The distance between the material domains was analysed using Fiji (ImageJ 1.54b). The average distance was determined by measuring the spatial separation between the material domains at three positions (left, middle and right) along the samples, covering roughly  $50 \text{ mm}$ .

### Fabrication of specimens for X-ray diffraction

Various resin formulations were used to fabricate different polymer specimens derived with three different initiators (Ru-1, Ru-2 and

Ru-3) (Extended Data Table 1). For this fabrication method,  $5.29 \text{ g}$  ( $6 \text{ ml}$ ) of COD was used. We use a  $15 \text{ mm} \times 60 \text{ mm} \times 3.3 \text{ mm}$  U-shaped high-temperature silicone rubber spacer between two  $1\text{-mm}$  thick glass slides for X-ray diffraction specimens. The specimen thickness was specifically chosen such that about 70% penetration of the X-ray source could be achieved. FROMP is initiated immediately by applying an electric current to a resistive wire placed along one edge of the mould. The power supply is turned off a few seconds after frontal propagation is observed and remains off for the remainder of the propagation. Specimens sat for  $24 \text{ h}$  under  $\text{N}_2$  at  $23.5 \text{ }^\circ\text{C}$  before removing the polymers from the glass mould. Samples were then cut to a  $1 \text{ cm} \times 4 \text{ cm}$  rectangular geometry and let to sit for another  $48 \text{ h}$  under  $\text{N}_2$  at  $23.5 \text{ }^\circ\text{C}$  before being placed in the freezer (about  $-20 \text{ }^\circ\text{C}$ ) to mitigate the evolution of the material domains before testing.

### Small- and wide-angle X-ray scattering

Simultaneous small- and wide-angle X-ray scattering experiments were conducted at beamline 12-ID-B, Advanced Photon Source, Argonne National Laboratory, using a Pilatus2M/Eiger9M detector (Dectris, Switzerland) for small-angle X-ray scattering and a Pilatus300K detector (Dectris, Switzerland) for wide-angle X-ray scattering. X-ray beams with an average photon energy of  $13.3 \text{ keV}$  were used. The sample-to-detector distances (SDDs) for small- and wide-angle X-ray scattering were approximately  $2 \text{ m}$  and  $0.46 \text{ m}$ , respectively. All calibrations for SDDs were performed using a silver behenate powder standard. The obtained scattering patterns were radially and azimuthally integrated using an Igor-based package, NIKA (ref. 42).

To determine the percentage distribution of the polymer chain orientation, we performed the following steps. First, the one-dimensional azimuthal plots acquired at each sample point were fitted using three Gaussian curves centring at  $-90^\circ$ ,  $0^\circ$  and  $90^\circ$ . We selected the higher height values from the Gaussian curves centred at  $-90^\circ$  and  $90^\circ$ . Using the selected height value, we calculated the percentage height ratio by including the height of the curve centred at  $0^\circ$ . The percentage height ratio is equivalent to the percentage distribution. In this data process, we fairly assumed that the one-dimensional azimuthal plots give rise to peaks only at  $-90^\circ$ ,  $0^\circ$  and  $90^\circ$ . To better illustrate the percentage distribution of the polymer chain orientation, violin plots were overlaid with data points using the software OriginPro. The kernel bandwidth was set to zero.

### Fabrication of specimens for mechanical testing

For this fabrication method,  $22.94 \text{ g}$  ( $26 \text{ ml}$ ) of COD was used and the initiator and inhibitor concentrations found in Extended Data Table 1 were scaled accordingly. Various resin formulations were used to fabricate different polymer specimens derived with the three initiators. The resin mixture was sonicated for  $10 \text{ min}$  until complete dissolution of the initiator and then transferred into the rectilinear mould. We used a  $60 \text{ mm} \times 65 \text{ mm} \times 4.2 \text{ mm}$  U-shaped high-temperature silicone rubber spacer between two  $1\text{-mm}$  thick glass slides for tensile specimens. The ambient temperature was set to  $T_0 = 20 \text{ }^\circ\text{C}$  for the Ru-1-derived specimens,  $T_0 = 30 \text{ }^\circ\text{C}$  for the Ru-2-derived specimens, and  $T_0 = 40 \text{ }^\circ\text{C}$  for the Ru-3-derived specimens. FROMP is initiated immediately by applying an electric current to a resistive wire placed along one edge of the mould. The power supply is turned off a few seconds after frontal propagation is observed and remains off for the remainder of the propagation. All specimens fabricated were left in the glass slides for  $24 \text{ h}$  before removing the specimen from the glass mould. We cut dog-bone specimens for tensile testing  $48 \text{ h}$  post-polymerization from the manufactured polymer specimen using an ASTM D638 Type V dimension die from Qualitest. Dog-bone specimens were then stored under  $\text{N}_2$  at  $23.5 \text{ }^\circ\text{C}$  for the remainder of their ageing process before quasi-static tensile testing. Ru-1 uniform specimens were left under  $\text{N}_2$  for  $48 \text{ h}$  ( $72 \text{ h}$  aged post-polymerization) and Ru-1 patterned specimens were left under  $\text{N}_2$  for  $120 \text{ h}$  ( $144 \text{ h}$  aged post-polymerization). Ru-2 and Ru-3 uniform



specimens were left under N<sub>2</sub> for 48 h (72 h aged post-polymerization) and the respective patterned specimens were left under N<sub>2</sub> for 96 h (120 h post-polymerization). Ru-3 ROMP oven-cured specimens were fabricated by placing the rectangular mould in an oven at 40 °C for 1.5 h. The specimens were left in the glass slides for 24 h before removing from the glass mould. We cut dog-bone specimens for tensile testing 24 h post-polymerization using an ASTM D638 Type V dimension die from Qualitest. The ROMP specimens were left under N<sub>2</sub> for 48 h (72 h aged post-polymerization). The respective heat of fusion for each specimen type at the time of testing can be found in Supplementary Table 5.

### Quasi-static tensile testing

Tensile tests were conducted using an Instron 5984 universal testing system equipped with a 5-kN load cell and a video extensometer under ambient conditions. Any compressive load introduced during the tightening of the grips of the frame was removed by loading the sample until the load read 0 N at 10% of the final testing rate. Tensile tests were performed under displacement control at a constant rate of 5 mm min<sup>-1</sup> until the samples failed. Young's modulus was calculated using the slope of the best-fit line for the stress–strain curve from 0.1% to 0.3% strain. The tensile strength of the sample was recorded as the maximum stress achieved during the test. Strain to failure was taken as the maximum strain the samples achieved at the point of failure. The strain energy density was calculated from the area under the curve of the stress–strain curve up to the point of failure. The error bars represent the 95% confidence intervals for  $n = 5$  calculated using a  $Z$ -score of 1.96.

### Thermomechanical characterization

The thermomechanical properties of uniform and patterned specimens derived from the three initiators were evaluated 24 h post-polymerization using dynamic mechanical analysis (DMA). These tests were performed on a TA Instruments Q800 equipped with a gas cooling accessory and tension clamps. Specimens were cut into rectangular samples 25 mm × 4 mm × 0.9 mm and the gauge length was maintained at 16 mm. DMA was performed in multi-frequency strain mode with an oscillation strain of 0.1% and a static force of 0.001 N. The temperature was increased linearly from –130 °C to 50 °C at 5 °C min<sup>-1</sup>. Data were obtained for a minimum of three specimens.

### Data availability

The main data supporting the findings of this study are available in the paper and its Supplementary Information. Other datasets generated or analysed during this study are available from the corresponding author on request. Source data are provided with this paper.

### Code availability

We performed the simulations using MOOSE, an open-source C++ finite-element framework developed at Idaho National Laboratory (<http://mooseframework.org>).

37. Kessler, M. R. & White, S. R. Cure kinetics of the ring-opening metathesis polymerization of dicyclopentadiene. *J. Polym. Sci. A* **40**, 2373–2383 (2002).
38. Cornell, S. W. & Koenig, J. L. The Raman spectra of polybutadiene rubbers. *Macromolecules* **2**, 540–545 (1969).
39. Hardis, R., Jessop, J. L. P., Peters, F. E. & Kessler, M. R. Cure kinetics characterization and monitoring of an epoxy resin using DSC, Raman spectroscopy, and DEA. *Compos. Part A Appl. Sci. Manuf.* **49**, 100–108 (2013).
40. Azo Materials. Silicone rubber <https://www.azom.com/properties.aspx?ArticleID=920> (Azo Materials, 2001).
41. Gaston, D., Newman, C., Hansen, G. & Lebrun-Grandié, D. MOOSE: a parallel computational framework for coupled systems of nonlinear equations. *Nucl. Eng. Des.* **239**, 1768–1778 (2009).
42. Ilavsky, J. *Nika*: software for two-dimensional data reduction. *J. Appl. Crystallogr.* **45**, 324–328 (2012).

**Acknowledgements** This work was supported as part of the REMAT EFRC, an Energy Frontier Research Center funded by the US Department of Energy, Office of Science, Basic Energy Sciences at the University of Illinois Urbana–Champaign under award no. DE-SC0023457. Y.K.G. and C.L. acknowledge support from the National Science Foundation under award no. CBET 2219305 (structural determination of polymer systems). Synchrotron X-ray experiments were performed at beamline 12-ID-B at the Advanced Photon Source (APS), Argonne National Laboratory. The use of APS was supported by the US Department of Energy (DOE), Office of Science, Office of Basic Energy Sciences, under contract no. DE-AC02-06CH11357. T.T. acknowledges support from the Scientific and Technological Research Council of Turkey (TUBITAK) under award no. 1059B191900205. We thank J. Cooper and B. Suslick for their discussions; D. Loudermilk for graphics assistance; the Materials Research Laboratory, the School of Chemical Sciences NMR Laboratory and the Beckman Institute for Advanced Science and Technology for use of their facilities and equipment. J.E.P. thanks the Beckman Institute for Advance Science and Technology for a Graduate Research Fellowship. Y.K.G. and L.E.R.K. acknowledge support from the PPG Materials Research Laboratory (MRL) Graduate Research Assistantship Award through the University of Illinois Urbana–Champaign. J.E.P. and A.S. acknowledge the NASA Illinois Space Grant Consortium Undergraduate Research Opportunity Program, Illinois Scholars Undergraduate Research Program and Semiconductor Research Corporation Undergraduate Research Program through the University of Illinois Urbana–Champaign. L.E.R.K. acknowledges support from the Minority PhD (MPHD) programme of the Alfred P. Sloan Foundation.

**Author contributions** N.R.S., P.H.G., J.S.M. and C.L. directed the research. N.R.S., P.H.G., J.E.P. and Y.G. conceived the idea. J.E.P., A.S., Y.K.G., L.E.R.K., J.J.L. and T.T. conducted the experiments. Y.G. and M.C. performed the numerical studies. J.E.P. wrote the paper, and all authors participated in the compilation of the figures, extended data and supporting information.

**Competing interests** The authors declare no competing interests.

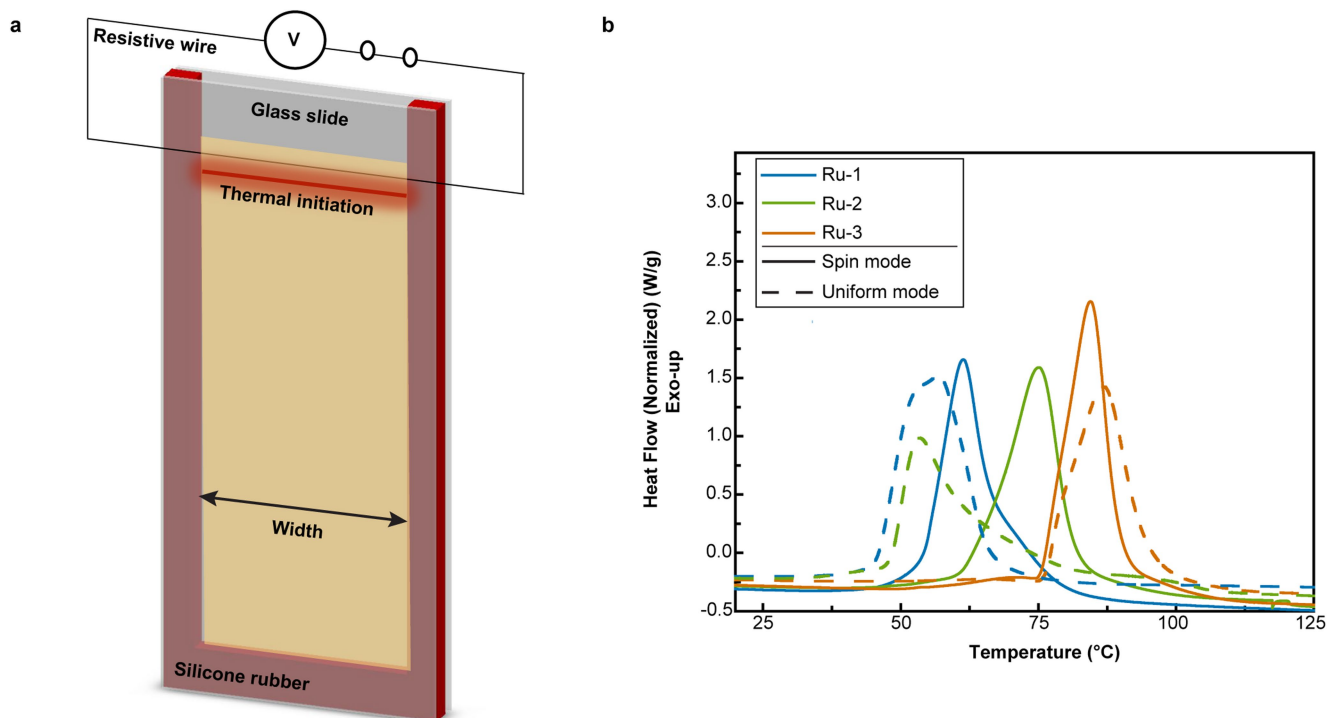
### Additional information

**Supplementary information** The online version contains supplementary material available at <https://doi.org/10.1038/s41586-024-07951-7>.

**Correspondence and requests for materials** should be addressed to Nancy R. Sottos.

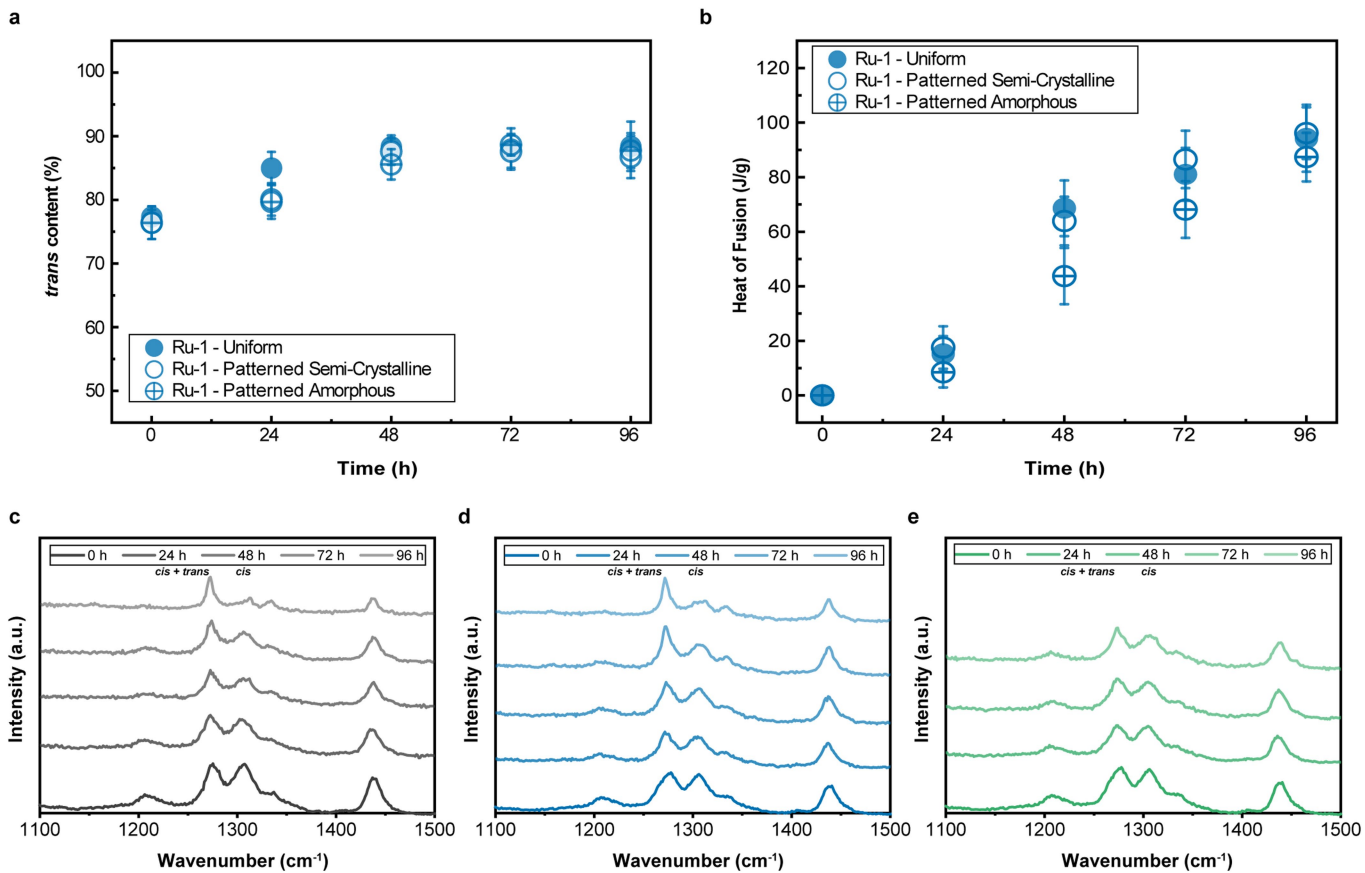
**Peer review information** *Nature* thanks Jeffrey C. Foster, Wenbing Hu and the other, anonymous, reviewer(s) for their contribution to the peer review of this work.

**Reprints and permissions information** is available at <http://www.nature.com/reprints>.



**Extended Data Fig. 1 | Experimental setup and characterization of COD curing.** **a**, Schematic representation of the experimental setup of the thermal frontal polymerization for both planar and nonplanar front dynamics. Initiation was achieved by powering a resistive wire in contact with one of the glass slides at the indicated location. **b**, Dynamic DSC traces for the

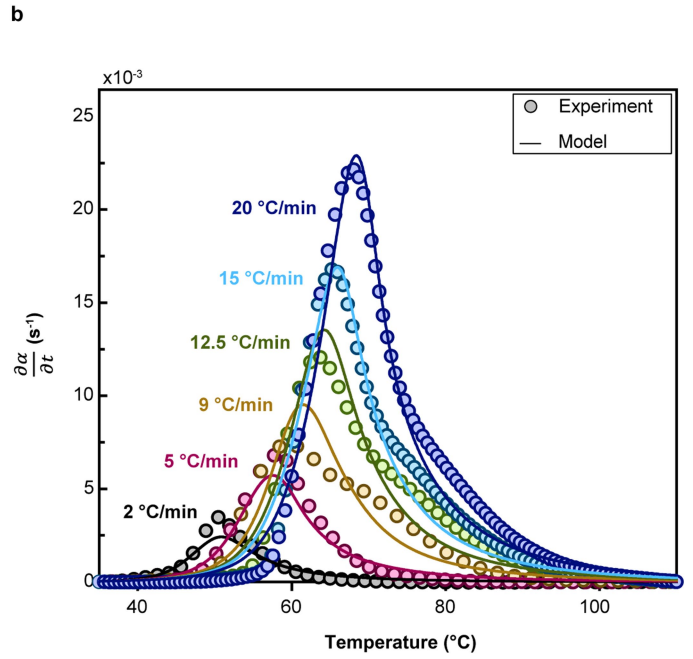
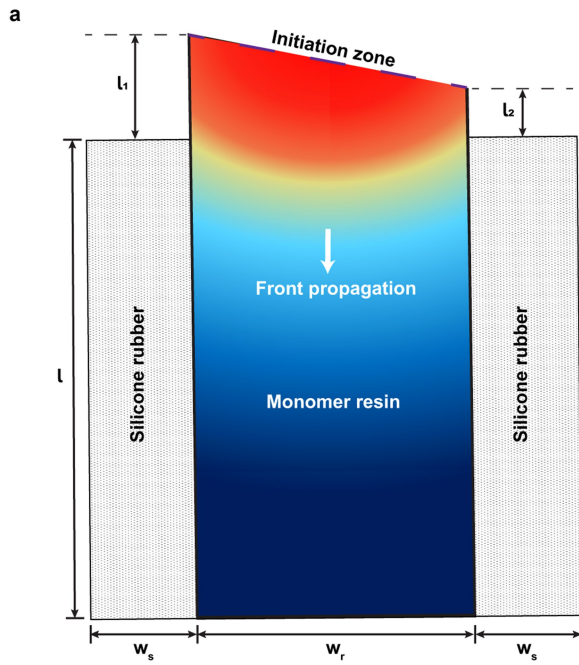
three initiator formulations (Ru-1, Ru-2, and Ru-3) that yield either spin mode or uniform mode of propagation. The solid curves represent the formulations that produce spin modes, and the dashed curves represent formulations that produce uniform modes. The formulations for each initiator and mode of propagation are presented in Extended Data Table 1.



**Extended Data Fig. 2 | Evolution of *trans* content of Ru-1 derived polymers.**

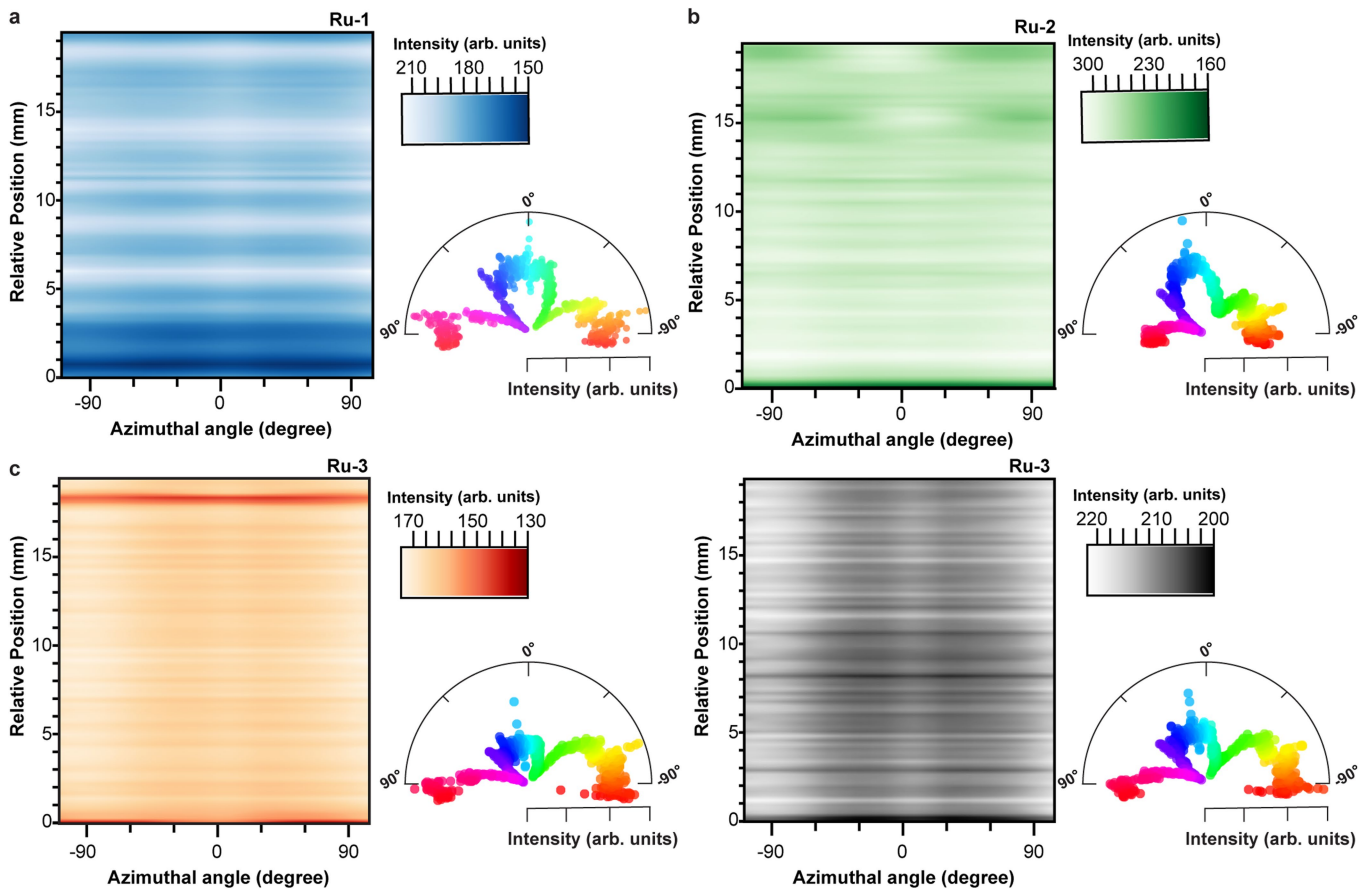
**a**, Average *trans* content as a function of time for uniform and patterned polymers derived from the Ru-1 initiator. **b**, Average heat of fusion as a function of time for uniform and patterned specimens. **(a, b)** Error bars represent the

maximum and minimum values ( $n = 3$ ). Raman spectra taken every 24 h for Ru-1 derived specimens **c**, Uniform polymer, **d**, Patterned polymer in the semi-crystalline domain, **e**, Patterned polymer in the amorphous domain.



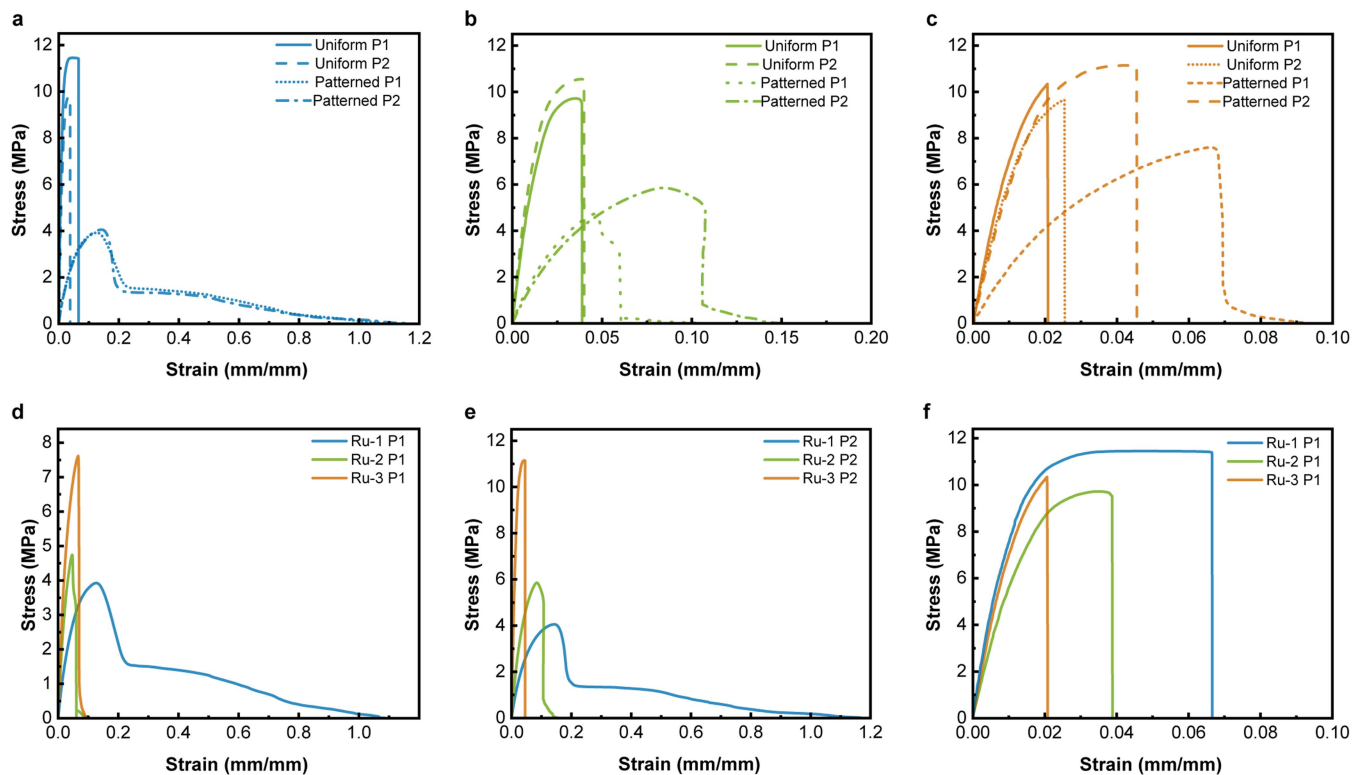
**Extended Data Fig. 3 | Numerical simulations of COD in a closed mold geometry.** **a**, Schematic representation of frontal polymerization in a closed mold geometry with silicone rubber and glass as boundaries. **b**, Cure profiles,  $d\alpha/dt$  ( $s^{-1}$ ) vs temperature ( $^{\circ}C$ ) at various ramp rates (2, 5, 9, 12.5, 15, 20  $^{\circ}C/min$ )

as measured experimentally by DSC and fit using an Arrhenius cure kinetic model that was used to extract the numerical parameters ( $E_a$ ,  $n$ , and  $m$ ) used in the simulations (Extended Data Table 2).



**Extended Data Fig. 4 | X-ray scattering of patterned and uniform polymers.** Contour plots of the azimuthal angle as a function of the relative position in the X2 scan direction and the corresponding polar plots of the average distribution of the polymer chain orientations along the scan direction. **a**, Ru-1 derived

patterned specimen fabricated at an ambient temperature of 25 °C. **b**, Ru-2 derived patterned specimen fabricated at an ambient temperature of 25 °C. **c**, Ru-3 patterned specimen fabricated at an ambient temperature of 25 °C. **d**, Ru-3 uniform specimen fabricated at an ambient temperature of 50 °C.



**Extended Data Fig. 5 | Tensile measurements of patterned and uniform polymers.** **a-f** representative stress-strain curves for uniform and patterned polymers derived from the three different ruthenium initiators. **d, e** are comparisons of the resulting patterned specimens in the P1 and P2 directions

and **f** is the comparison of the uniform specimens in the P1 direction. Corresponding values of the mechanical properties can be found in Extended Data Table 4.

**Extended Data Table 1 | Initiator and inhibitor concentrations for spin and uniform modes of front propagation and the corresponding front velocity, maximum front temperature, and heat of reaction for a 5.29 g (6 mL) sample**

Initiator	Mode of Front Propagation	Mass of initiator (mg)	Initiator Concentration (mmol)	Volume of Inhibitor ( $\mu$ L)	Inhibitor Concentration (mmol)	Molar equiv. of Inhibitor to Initiator	$v_f^\dagger$ (mm/sec)	$T_{max}$ ( $^\circ$ C)	$H_r^\ddagger$ (J/g)
Ru-1	Spin	7.68	0.0090	5.0	0.018	2.0	0.45 $\pm$ 0.03	159 $\pm$ 4	298.2 $\pm$ 4.5
Ru-1	Uniform	7.68	0.0090	2.5	0.0092	1.0	0.41 $\pm$ 0.01	158 $\pm$ 6	305.6 $\pm$ 6.3
Ru-2	Spin	7.20	0.0087	4.0	0.015	1.7	0.28 $\pm$ 0.03	152 $\pm$ 3	290.8 $\pm$ 5.8
Ru-2	Uniform	7.20	0.0087	2.0	0.0074	0.85	0.33 $\pm$ 0.02	158 $\pm$ 2	303.4 $\pm$ 7.1
Ru-3	Spin	8.40	0.0089	2.4	0.0089	1.0	0.26 $\pm$ 0.02	153 $\pm$ 1	304.9 $\pm$ 5.9
Ru-3	Uniform	8.40	0.0089	1.2	0.0044	0.50	0.23 $\pm$ 0.02	157 $\pm$ 2	306.3 $\pm$ 8.5
Ru-3 <sup>*</sup>	Spin	16.80	0.018	1.2	0.0044	0.25	0.28 $\pm$ 0.03	156 $\pm$ 2	305.1 $\pm$ 7.6
Ru-3	ROMP Uniform	8.40	0.0089	1.2	0.0044	0.50	-	-	306.3 $\pm$ 8.5

$v_f$ : front speed;  $T_{max}$ : maximum front temperature;  $H_r$ : heat of reaction.

Reported values represent the average, with error bars indicating the maximum and minimum values for a sample size of  $n=3$ .

<sup>\*</sup>Represents the resin formulation for successful spin mode propagation of Ru-3 at ambient temperatures below 40 $^\circ$ C.

<sup>†</sup>Front temperatures and velocities are highly dependent on the material and geometrical conditions used for manufacturing. The values reported here correspond to the experimental conditions described in the Methods section.

<sup>‡</sup>The heat of reaction was measured from differential scanning calorimetry dynamic scans at a rate of 5 $^\circ$ C/min.

# Article

Extended Data Table 2 | Physical and thermal properties of COD and silicone rubber used in numerical modeling

	$\kappa$ (W m <sup>-1</sup> K <sup>-1</sup> )	$\rho$ (kg m <sup>-3</sup> )	$H_f$ (J g <sup>-1</sup> )	$C_p$ (J kg <sup>-1</sup> K <sup>-1</sup> )	$A$ (s <sup>-1</sup> )	$E$ (kJ mol <sup>-1</sup> )	$n$	$m$
COD (r)	0.133	882	259	1,838	1.57 x 10 <sup>17</sup>	117.45	2.60	0.83
Silicone rubber (s)	1.0	1,500	-	1,200	-	-	-	-



**Extended Data Table 3 | Comparison of the percent distribution of polymer chains for specimens derived from the three ruthenium initiators and by different modes of front propagation**

Initiator	Specimen Type	Ambient Temperature (°C)	Percent Distribution $\theta = 0^\circ$	Percent Distribution $\theta = \pm 90^\circ$
Ru-1	Patterned	25	45.5	54.5
Ru-2	Patterned	25	41.6	58.4
Ru-3	Patterned	25	36.2	63.0
Ru-1	Uniform	20	33.0	67.0
Ru-2	Uniform	30	44.0	56.0
Ru-3	Uniform	50	41.3	58.7

# Article

**Extended Data Table 4 | Comparison of the mechanical properties for specimens derived from the three ruthenium initiators and by different modes of front propagation**

Initiator	Specimen Type	Specimen Orientation	Ambient Temperature (°C)	Domain Spacing (mm)	Elastic Modulus (MPa)	Tensile Strength (MPa)	Strain Energy Density (MJ/m <sup>3</sup> )	Strain to Failure (mm/mm)
Ru-1	Patterned	1	20	1.6 ± 0.2	91 ± 8	4.2 ± 0.2	1.42 ± 0.33	1.0 ± 0.2
Ru-1	Patterned	2	20	1.6 ± 0.2	85 ± 9	4.0 ± 0.2	1.49 ± 0.23	1.1 ± 0.1
Ru-2	Patterned	1	30	0.6 ± 0.1	199 ± 13	5.2 ± 0.4	0.21 ± 0.07	0.1 ± 0.02
Ru-2	Patterned	2	30	0.6 ± 0.1	182 ± 14	5.8 ± 0.7	0.43 ± 0.15	0.1 ± 0.07
Ru-3	Patterned	1	40	1.0 ± 0.1	275 ± 25	7.6 ± 0.5	0.43 ± 0.14	0.1 ± 0.005
Ru-3	Patterned	2	40	1.0 ± 0.1	730 ± 57	11.2 ± 0.5	0.50 ± 0.13	0.1 ± 0.01
Ru-1	Uniform	1	20	N/A	819 ± 87	11.7 ± 0.5	0.59 ± 0.28	0.1 ± 0.01
Ru-1	Uniform	2	20	N/A	625 ± 35	10.0 ± 1.0	0.29 ± 0.07	0.04 ± 0.004
Ru-2	Uniform	1	30	N/A	633 ± 27	9.8 ± 0.1	0.27 ± 0.05	0.04 ± 0.006
Ru-2	Uniform	2	30	N/A	674 ± 58	10.2 ± 0.7	0.32 ± 0.11	0.04 ± 0.01
Ru-3	Uniform	1	40	N/A	803 ± 88	10.6 ± 0.9	0.17 ± 0.02	0.03 ± 0.002
Ru-3	Uniform	2	40	N/A	761 ± 84	10.0 ± 0.4	0.18 ± 0.02	0.03 ± 0.004
Ru-3	ROMP Uniform	1	40	N/A	517 ± 33	9.0 ± 0.4	0.27 ± 0.06	0.04 ± 0.007
Ru-3	ROMP Uniform	2	40	N/A	528 ± 27	8.4 ± 0.5	0.18 ± 0.06	0.04 ± 0.007

Reported values and error bars represent the average and 95% confidence interval, respectively, for a n=5.